Fabrication of Porous Phosphate/Carbonate Composites: Smart Fertilizer with Bimodal Controlled-Release Kinetics and Glyphosate Adsorption Ability

Pratchayaporn Yukhajon, Titikan Somboon, and Sira Sansuk*

Read Online

ACCESS | Metrics & More | Article Recommendations | SI Supporting Information

ABSTRACT: A simple method to prepare phosphate/carbonate composites for use as porous sponge-like phosphate fertilizers (ps-PO_4Fs) is presented. The composites ps-PO_4Fs were prepared by ion-exchange implantation of phosphate onto the surface of vaterite-phase calcium carbonate ($CaCO_3$) microparticles. The ps-PO_4Fs obtained under the optimized conditions were found to contain a nanoscale porous network of calcium phosphate covering the $CaCO_3$ support. In addition, ps-PO_4Fs exhibited two distinct phosphate release modes having different kinetics: a fast-release step over the initial 24 h period following a parabolic diffusion model, indicating controlled diffusion from external surfaces/edges, and a second slow-release step over the course of a month following the Ritger−Peppas model, indicating the release and diffusion of phosphate adsorbed at specific sites. The ps-PO_4Fs also adsorbed glyphosate well because of their porous structure and large surface area. However, glyphosate adsorption prevented phosphate release at concentrations greater than 10 mg L^{-1}. The ps-PO_4Fs were tested for their effects on plant growth and showed effects similar to commercial fertilizers. In summary, these smart, eco-friendly, and multifunctional fertilizers having two-stage phosphate release could enable the application of lower amounts of fertilizer and remove excess glyphosate from the environment.
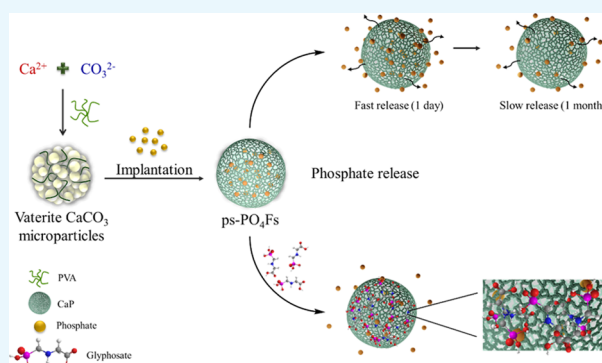
1. INTRODUCTION

Phosphorus is one of the most important macronutrients for crop and plant growth.[1] It is commonly utilized in its oxidized and hydrated forms such as $H_2PO_4^-$, HPO_4^{2-}, and PO_4^{3-}, depending on the pH of the growth media.[2,3] For example, one commercially available phosphate fertilizer, diammonium phosphate (DAP), has a relatively high solubility in an aqueous medium, but the take-up of DAP by plants is low. Therefore, the dose applied to crop-growing areas is typically much higher than that necessary to ensure healthy plant growth.[4,5] The incorrect use of DAP and other fertilizers can reduce their efficiency by increasing production costs while not proportionally increasing yields. Furthermore, excessive phosphate use can cause serious environmental damage, including water pollution through the runoff of phosphate from the soil into the surface water.[6] As a solution, controlled-release fertilizer (CRF) systems could prevent the excessive application of phosphate and improve fertilizer effectiveness and efficiency.[7] However, the reported CRF systems generally exhibit a single controlled-release step and cannot be adopted in large-scale agriculture practices because of the high cost of commercial production. Thus, it is important to develop a simple method for the preparation of CRF systems with multistep release mechanisms to benefit plant growth at different stages.

Glyphosate (N-(phosphonomethyl)glycine) is a very widely used organophosphate herbicide. It is water-soluble, non-volatile, and nonphotodegradable. The use of glyphosate to control and inhibit weed growth in agriculture has increased considerably in recent years.[8,9] Most farmers apply herbicides at doses higher than recommended, which, like the overuse of fertilizers, results in environmental damage. In particular, because of its low photodegradability, glyphosate is retained in the soil and can be released into the aquatic environment through leaching.[10−12] Moreover, the excess glyphosate can accumulate in the soil because its functional groups, including phosphonate ($-PO(OH)_2$), amino ($-NH-$), and carboxyl ($-COOH$) groups, form interactions with minerals, resulting in its adsorption and retention.[13] Importantly, glyphosate is
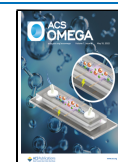
classified as "probably carcinogenic", so its removal from the environment is very important.

To date, various carriers have been used in slow-release fertilizer systems, including encapsulated materials,[14] hydrogels,[15,16] and polymers.[17,18] Although these carrier materials enable the controlled release of fertilizers, the production process is difficult and expensive and requires the use of organic solvents. In addition, organic frameworks (MOFs) have been utilized in the preparation of fertilizers.[19] Although exhibiting efficiency in their controlled release, the practical use is still questionable since their residue can be left contaminating the environment and crops. Recently, sustainable materials, such as layered double hydroxides (LDHs), have been developed for controlled-release systems.[1,20] Among inorganic materials, calcium carbonate ($CaCO_3$) is naturally abundant and possesses some outstanding properties for environmental applications, such as nontoxicity and high stability. So far, there have been reports of the application of $CaCO_3$ in controlled-release systems.[21,22] For example, $CaCO_3$ nanoplates have been prepared through a solvothermal method and employed as a carrier for the sustained release of drugs.[23] The resulting $CaCO_3$ nanoplates inhibited the initial burst release, but the synthetic process requires organic solvents, which increases the risk of contamination. For agricultural applications, starch-regulated $CaCO_3$ particles have been fabricated by coprecipitation and used as an efficient system for the slow release of the herbicide prometryn.[24] However, it has proven challenging to develop smart, sustainable, and well-performing systems capable of the controlled release of fertilizers and the adsorption of herbicides using simple methods and at a low cost.

Therefore, the aim of this study is to address the aforementioned issues by focusing on the development of a smart, eco-friendly, and multifunctional system having efficient controlled-release properties for use in agriculture. Herein, phosphate/carbonate composites with a nanoscale porous network structure were designed to target agricultural use as an efficient fertilizer with the ability to adsorb herbicides. The process involves the synthesis of $CaCO_3$ particles by precipitation using poly(vinyl alcohol) (PVA) as the regulator, and the effect of PVA concentration and reaction time on the surface morphology and crystal phase of the $CaCO_3$ particles have been examined. The composites were fabricated by the passive implantation of phosphate onto the prepared $CaCO_3$ supports. The resulting porous sponge-like phosphate fertilizers (ps-PO_4Fs) were then tested for their phosphate release profiles. In addition, different mathematical models were applied to model the release kinetics. Furthermore, the phosphate release of ps-PO_4Fs was tested in the presence of different concentrations of glyphosate and the use for plant growth was demonstrated to assess their agricultural applications.

2. MATERIALS AND METHODS

2.1. Chemicals and Reagents. All chemicals were of analytical grade and used as received without further purification. Calcium acetate (($CH_3COO)_2Ca$) and PVA were purchased from Loba Chemie (Thailand). Glyphosate ($C_3H_8NO_5P$) in acid form was obtained from Dr. Ehrenstorfer GmbH (Germany). Potassium dihydrogen orthophosphate (KH_2PO_4) and sodium carbonate (Na_2CO_3) were acquired from BDH Prolabo (U.K.). DAP was purchased from a local market in Khon Kaen Province (Thailand). Deionized water

was produced using a RiO$_s$ Type-I Simplicity 185 (Millipore) and had a resistivity of 18.2 MΩ cm and a conductivity of 0.055 μS cm^{-1}. This water was used throughout the study. Stock solutions of 2.0 M KH_2PO_4 and 500 mg L^{-1} glyphosate were prepared by dissolving the appropriate amounts of each compound in 100 mL of deionized water.

2.2. Synthesis of $CaCO_3$ Particles. The synthesis process of $CaCO_3$ particles was adapted from the previous report.[24] In this work, PVA with a molecular weight of ~115,000 g mol^{-1} and a degree of polymerization of 1700−1800 was used as a structural regulator. In a typical procedure, 1.50 g of PVA was added to 100 mL of deionized water and heated to 60 °C with stirring at 300 rpm until the solution became transparent. The solution was then allowed to cool to room temperature. Then, 1.58 g of ($CH_3COO)_2Ca$, which was used as the calcium ion source, was added to the solution and stirred continuously for 30 min. Next, 100 mL of a 0.1 M Na_2CO_3 solution, which was used as a source of carbonate ions (CO_3^{2-}), was slowly dropped for 5 min into the mixture and stirred for 12 h. Finally, when a suspension was formed, the particles were filtered out, washed with deionized water, and dried at 60 °C in an oven until no mass change was observed. The conditions for the synthesis of $CaCO_3$ particles were optimized by varying the amount of PVA and reaction time.

2.3. Fabrication of ps-PO_4Fs. The ps-PO_4Fs are phosphate/carbonate composites prepared through the impregnation of phosphate onto the surface of the as-prepared $CaCO_3$ particles. Briefly, 1.0 g of the $CaCO_3$ particles prepared by the optimized synthetic method was soaked in 10 mL of 0.5 M KH_2PO_4 in a sealed beaker. The suspension was continuously stirred at 300 rpm during the implantation process. The composites were obtained by filtration and drying at 60 °C for 12 h. The phosphate content in ps-PO_4Fs, expressed as the implantation content (%IC), was estimated using eq 1.

$$\%IC = [(W_2 - W_1)/W_2] \times 100 \tag{1}$$

where W_1 is the weight of $CaCO_3$ particles and W_2 is the weight of ps-PO_4Fs. Thus, $W_2 - W_1$ is the weight of phosphate found in ps-PO_4Fs. The effects of KH_2PO_4 concentration and implantation time on the prepared ps-PO_4Fs were studied in the ranges of 0.2−2.0 M and 0.5−24 h, respectively. Moreover, phosphate composite fertilizers (PCFs) were also prepared by the physical mixing of KH_2PO_4 powder and the optimized $CaCO_3$ particles to compare the release efficiency of the ps-PO_4Fs.

2.4. Study of Phosphate Release from ps-PO_4Fs. The phosphate release behavior of the prepared ps-PO_4Fs was studied in a batch system as follows. First, 100 mg of ps-PO_4Fs was added to 50 mL of deionized water. The resulting suspension was stirred at 300 rpm and room temperature. Then, at given intervals, 1 mL of the suspension was withdrawn and centrifuged at 6000 rpm for 5 min to achieve phase separation. The precipitate was collected, dispersed in 1 mL of deionized water, and then placed into the original system. The phosphate content in the supernatant was determined based on the phosphomolybdenum blue reaction.[25] For the absorption measurements, the absorbance at 730 nm was used to evaluate the phosphate concentration. The phosphate release characteristics of the ps-PO_4Fs are reported in terms of the cumulative release ratio (%CRR), as given by eq 2.
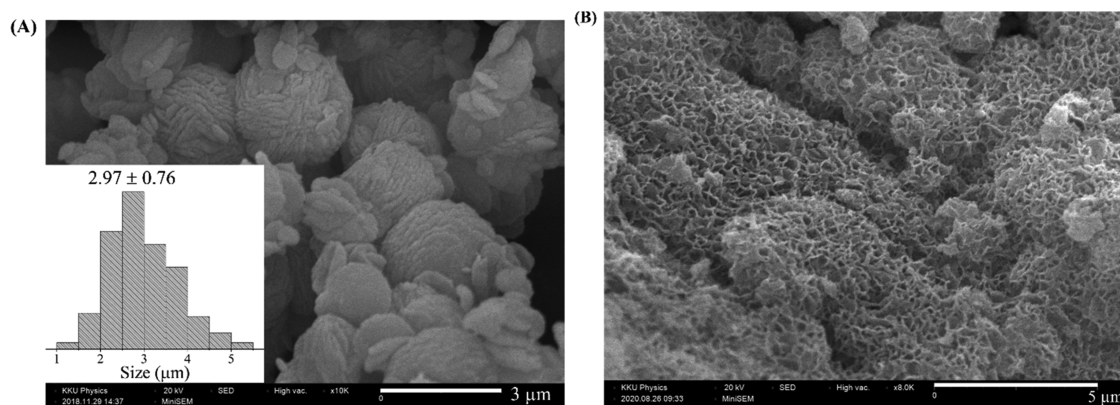
Figure 1. SEM images of (A) the optimal-CaCO$_3$ (3 μm scale bar) with particle size distribution (inset) and (B) ps-PO$_4$Fs (5 μm scale bar).

$$\%CRR = \left(\frac{C_t \cdot V_{\text{total}} + \sum_0^{t-1} C_t \cdot V_t}{m_0} \right) \times 100\% \qquad (2)$$

where C_t and V_t are the concentration of phosphate and the volume (1 mL) of the solution taken from the system at time t, respectively; V_{total} is the total volume (50 mL) of the solution in the studied system; and m_0 is the weight (mg) of phosphate present in the ps-PO$_4$Fs. For comparison, the release characteristics of KH$_2$PO$_4$, DAP, and PCFs with equivalent amounts were also investigated using a similar procedure. In addition, the release of phosphate from the ps-PO$_4$Fs in the presence of glyphosate at various concentrations was tested. All tests were performed in triplicate.

In addition, the release kinetics of ps-PO$_4$Fs were investigated using various models. The selected mathematical models are first-order kinetics, Higuchi, Ritger−Peppas, and parabolic diffusion, as given by eqs 3−6.[24]

$$\ln (1 - M_t/M_\infty) = -kt \qquad (3)$$

$$M_t/M_\infty = kt^{1/2} \qquad (4)$$

$$M_t/M_\infty = kt^n \qquad (5)$$

$$(M_t/M_\infty)/t = kt^{-1/2} + b \qquad (6)$$

where M_t/M_∞ is the release ratio of phosphate at time t (h); k is the kinetic constant; n is the diffusion exponent, for which $n \leq 0.43$ indicates Fickian diffusion and $0.43 < n < 1.0$ indicates non-Fickian or anomalous transport; and b is a constant.

2.5. Glyphosate Capture of ps-PO$_4$Fs. Having a porous structure, the ps-PO$_4$Fs can adsorb glyphosate. In a typical experiment, 100 mg of ps-PO$_4$Fs was dispersed in 50 mL of 100 mg L^{-1} aqueous glyphosate with continuous stirring. Subsequently, 1 mL of the suspension was withdrawn at intervals and centrifuged at 6000 rpm for 5 min to complete the separation. The residual amount of glyphosate in the supernatant was quantified using the absorbance at 570 nm to calculate the capture efficiency (%CE), as given by eq 7.

$$\%CE = [(A_0 - A_t)/A_0] \times 100 \qquad (7)$$

where A_0 and A_t are the absorbances of glyphosate before and after capture at any given time, respectively. All experiments were performed in triplicate. The capture of glyphosate from an aqueous solution by the optimized CaCO$_3$ adsorbent was also investigated in the same manner.

2.6. Test of ps-PO$_4$Fs for Plant Growth. The feasibility of using the ps-PO$_4$Fs for plant growth was also evaluated. In this study, *Ipomoea aquatica*, one of the most widely consumed vegetables in Thailand, was selected as the model plant. First, seeds of *I. aquatica* were placed inside a cuboidal sponge (5.08 cm × 5.08 cm × 2.54 cm) in a beaker containing 200 mL of the ps-PO$_4$Fs suspension. The amount of fertilizer was fixed at 10 mg for every test. For comparison, the optimized CaCO$_3$, PCFs, KH$_2$PO$_4$, DAP, and deionized water (control group) were used for plant growth under the same conditions. The plants were photographed, and their heights and root lengths were recorded after 1 week. All tests were performed in triplicate at the solution temperature of 29.2 ± 1.6 °C.

2.7. Characterization. The functional groups of the samples were studied using Attenuated total reflection-Fourier transform infrared spectroscopy (ATR-FTIR, Bruker, TEN-SOR27) by scanning from 4000 to 500 cm^{-1}. The samples were dried and ground to fine powder before the measurement. The surface morphology was observed using scanning electron microscopy (SEM, Mini-SEM, LEO, SNE-4500M) at an acceleration voltage of 20 kV. The samples were dried and placed on adhesive carbon disks and finally gold-coated before measurement. Thermogravimetry was carried out on a HITACHI STA7200 instrument at a heating rate of 10 °C min^{-1} between 30 and 800 °C in a N$_2$ atmosphere at a flow rate of 100 mL min^{-1}. The measurements were carried out in open alumina pans using α-Al$_2$O$_3$ as the standard reference material. The particle size distribution was determined using the ImageJ software. The crystal structures were confirmed by powder X-ray diffractometry (XRD) measurements using a PANalytical EMPYREAN diffractometer and monochromatic Cu Kα radiation (λ = 1.5406 Å) in the 2θ range of 10−60°. The samples were ground to a fine powder prior to the XRD measurement. The Brunauer−Emmett−Teller (BET) specific surface area and porosity were studied at 77 K using a BELSORP-miniX gas adsorption analyzer. The surface charges of the samples in aqueous suspension were determined by zeta potential measurement using a Zetasizer Nano ZS (Malvern Instruments Ltd, Malvern, U.K.). Ultraviolet−visible (UV−vis) measurements were carried out for the quantitative analysis of phosphate and glyphosate using an Agilent Cary 60 UV−vis spectrophotometer with 1.0 cm quartz cells.

3. RESULTS AND DISCUSSION

3.1. CaCO$_3$ Particles. The CaCO$_3$ particles were synthesized by reacting calcium ions (Ca^{2+}) and carbonate

ions (CO_3^{2-}) in the presence of PVA as a regulator at 27 °C in the ambient atmosphere. Two key factors that could affect the formation of $CaCO_3$ particles, the reaction time and PVA concentration, were investigated, and the $CaCO_3$ samples were fully characterized. The SEM results in Figures S1 and S2 reveal that, if the PVA content and reaction time were insufficient, particles with irregular morphologies were obtained. However, the use of an excess PVA content led to PVA residue on the as-prepared particles. After contemplating both factors, the optimal conditions for the synthesis of $CaCO_3$ particles (denoted "optimal-$CaCO_3$") were found to be 15 mg mL^{-1} of PVA and 12 h of reaction time. Under these synthetic conditions, mostly spherical particles having an average diameter of approximately 3 μm were obtained, as illustrated in Figure 1A. The XRD result in Figure S3 shows that these microparticles were $CaCO_3$ with a hexagonal vaterite-phase structure, consistent with JCPDS No. 96-900-7476.[26] Specifically, the diffraction peaks at 2θ = 20.91, 24.87, 27.03, 32.71, 40.61, 42.56, 43.80, 49.01, 49.92, 51.03, and 55.73° correspond to the (002), (010), (011), (012), (013), (004), (110), (112), (014), (020), and (022) planes of hexagonal vaterite phase.[26] In addition, the disappearance of the characteristic peak of calcite at 2θ = 30° indicates the purity of vaterite $CaCO_3$ microparticles.

The FTIR measurements were carried out to understand the formation mechanism of the $CaCO_3$ microparticles. As presented in Figure S4 and information in Table S1, the FTIR spectrum of PVA contains a characteristic peak at 3280 cm^{-1}, which originates from the stretching vibration of free hydroxyl groups.[27,28] A sharp peak was observed at 2937 cm^{-1} arising from the C−H stretching vibrations of alkyl groups.[27,28] The peak at 1710 cm^{-1} can be assigned to the stretching of the C=O groups in acetate.[27,28] The peak at 1427 cm^{-1} corresponds to the bending vibration of the CH_2 groups.[27,28] Two peaks at 1140 and 1086 cm^{-1} are attributed to the C−O stretching vibrations.[27,28] Additionally, the peaks at 918 and 844 cm^{-1} are ascribed to the −CH_2 rocking and C−C stretching, respectively, vibrations of PVA.[27,28] The characteristic peaks of the $CaCO_3$ particles were observed at 1435 and 1087 cm^{-1}, corresponding to the asymmetric and symmetric carbonate stretching vibrations, respectively. The other peaks at 874 and 745 cm^{-1} result from the out-of-plane and in-plane bending vibrations of carbonate, respectively.[29] These results confirm that the obtained $CaCO_3$ belongs to the vaterite phase. In addition, a broad peak was observed at 3335 cm^{-1} and can be ascribed to the −OH stretching of PVA. In addition, the main peak at 1710 cm^{-1}, corresponding to the carbonyl stretching of PVA, shifts to 1670 cm^{-1} (broad) in the $CaCO_3$ particles (Table S1). This shift could be attributed to the chelation of Ca^{2+} by the C=O groups in PVA molecules during $CaCO_3$ particle formation. Moreover, the peak at 1765 cm^{-1} of the $CaCO_3$ particles probably relates to the C=O stretching vibration of the acetate group, which is considered as the residual of PVA.[30,31]

In addition, thermogravimetry was performed to determine the composition and stability of the obtained $CaCO_3$ particles. As shown by the thermogram (TG) of $CaCO_3$ particles in Figure S5, four stages of weight loss occurred. The first weight loss between 25 and 120 °C results from the loss of water molecules physically adsorbed on the $CaCO_3$ particles. The second mass loss between 120 and 380 °C corresponds to the decomposition of acetate and hydroxyl groups of PVA embedded in the particles. The third mass loss between 380

and 500 °C is a result of the fracture of the main chain of PVA and the subsequent decomposition of the polymer framework at temperatures above 450 °C.[32] The last mass loss from 500 to 750 °C could be related to the decomposition of $CaCO_3$. Therefore, the PVA molecules, as well as acetate, used as a source of Ca^{2+}, were retained in the as-prepared $CaCO_3$ particles after synthesis. These results confirm a successful synthesis of vaterite $CaCO_3$ particles with the use of PVA, which is favorable since it is water-soluble, biodegradable, nontoxic, and cheap. The optimal-$CaCO_3$ particles were further employed as supports for the fabrication of ps-PO_4Fs.

3.2. Composites ps-PO_4Fs. The ps-PO_4Fs were fabricated by simple impregnation of phosphate on the surface of the optimal-$CaCO_3$ supports at room temperature and ambient conditions. The effects of phosphate concentration and implantation time were also investigated. As displayed in Figure S6, the determined values of %IC increased significantly when increasing the concentrations of KH_2PO_4 with a linear equation of $y = 16.42155x + 1.5529$ and regression coefficient (R^2) of 0.9578. This can be attributed to the substitution of CO_3^{2-} in the $CaCO_3$ structure with $H_2PO_4^{-}$/HPO_4^{2-} ions by anion exchange.[33,34] Specifically, $H_2PO_4^{-}$/HPO_4^{2-} ions could bind with Ca^{2+} ions to form dicalcium phosphate dihydrate ($CaHPO_4 \cdot 2H_2O$, DCPD), which was deposited on the surface of $CaCO_3$, as confirmed by matching the XRD pattern with JCPDS No. 00-002-0085.[35] Despite the enhanced impregnation of phosphate in the composites, the phase of the optimal-$CaCO_3$ particles could change to calcium phosphate (CaP) at higher phosphate concentrations. The XRD results in Figure S7 indicated the reduced intensities of the characteristic peaks of $CaCO_3$ vaterite phase, if >0.5 M KH_2PO_4 was used. Thus, 0.5 M KH_2PO_4 solution was selected as an optimal concentration for the fabrication of the composites.

The effect of the reaction time on the implantation capacity was studied using a 0.5 M KH_2PO_4 solution. The results in Figure S8 showed that %IC increased during the first 1 h, possibly because of ion exchange between CO_3^{2-} ions and $H_2PO_4^{-}$/HPO_4^{2-} ions. However, the %IC decreased after impregnation for 6 h, probably because of the reversible nature of the ion-exchange reaction ($CO_3^{2-} \leftrightarrow H_2PO_4^{-}$/$HPO_4^{2-}$).[36] However, this reaction was not completed after 6 h, as confirmed by the characteristic FTIR bands in Figure S9 and the XRD pattern in Figure S10. In other words, there was a tendency toward DCPD formation between 0.5 and 6 h, based on the characteristic FTIR peaks and XRD patterns.[37] Figure S11 presents the comparison of XRD patterns and FTIR spectra between DCPD powder and the optimal-$CaCO_3$ after treatment with 0.5 M KH_2PO_4 solution for 6 h. Information of FTIR vibrational band position and associated bonding is also given in Table S2. These results confirm the presence of DCPD deposited on the surface of optimal-$CaCO_3$ support. After 12 h of impregnation, the sample produced FTIR peaks consistent with carbonate hydroxyapatite, possibly as a result of equilibrium ion exchange between CO_3^{2-} and OH^- and PO_4^{3-} ions in the hydroxyapatite (HAp) lattice (reversible ion exchange) via A-type and B-type substitution, respectively.[38,39] However, the optimal-$CaCO_3$ phase remained during phosphate implantation. If the implantation time was prolonged to 24 h, %IC increased, which corresponded to an enhanced percentage of HAp in the composites, as seen in the FTIR spectra (Figure S9) and XRD patterns (Figure S10). However, a change of the $CaCO_3$ phase in the composites was observed as a result of more dissolution of $CaCO_3$ particles
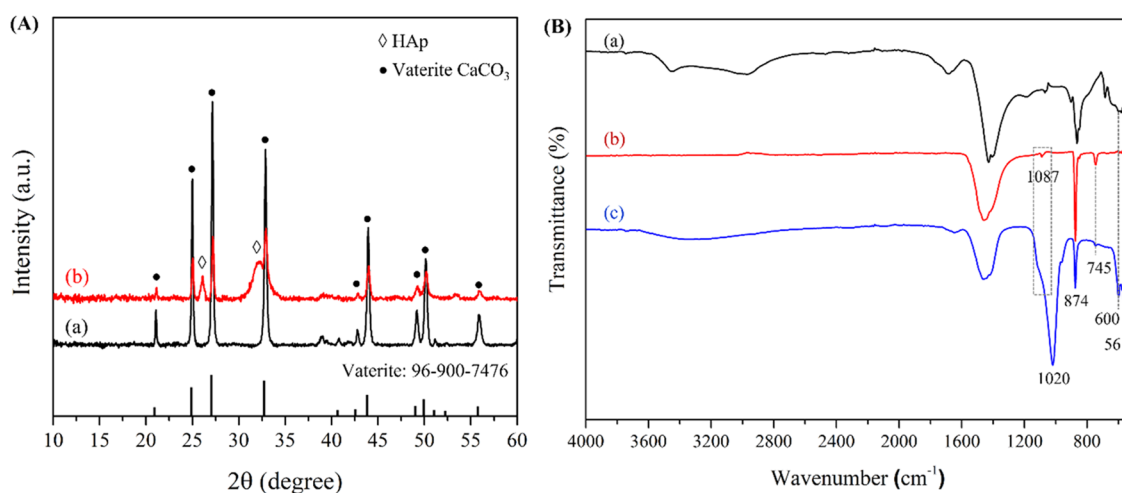
Figure 2. (A) XRD patterns of (a) optimal-CaCO$_3$ and (b) ps-PO$_4$Fs. (B) FTIR spectra of (a) KH$_2$PO$_4$ powder, (b) optimal-CaCO$_3$, and (c) ps-PO$_4$Fs.
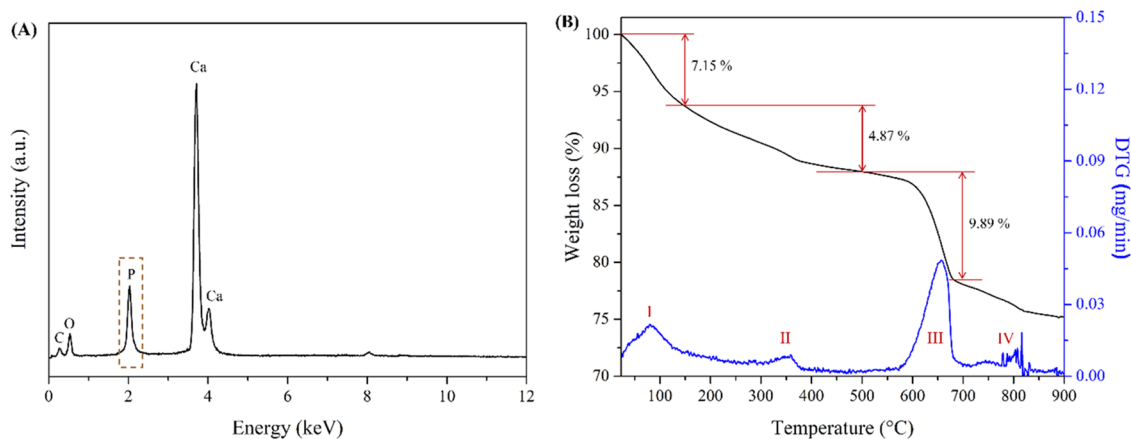

Figure 3. (A) EDX pattern and (B) TGA/differential thermogravimetric (DTG) curves of the ps-PO$_4$Fs.
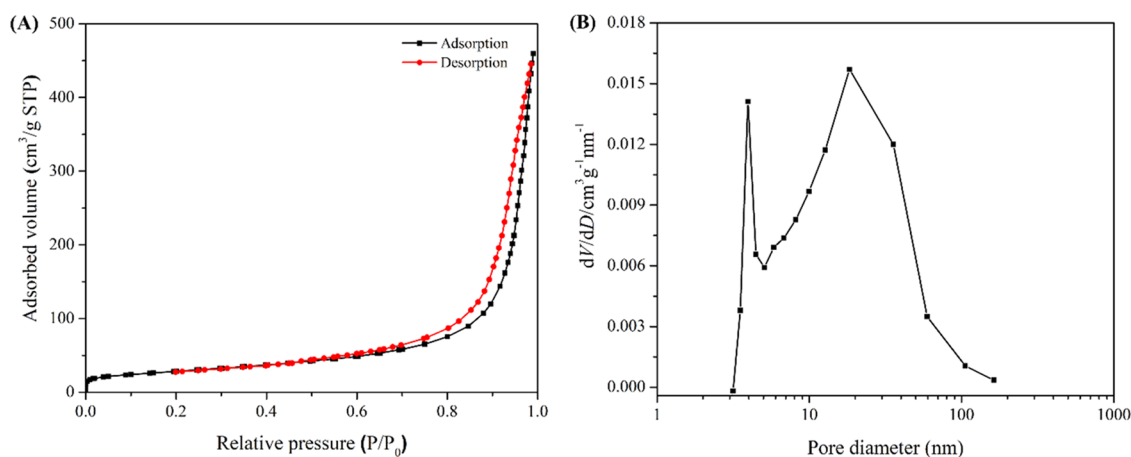
Figure 4. (A) N$_2$ absorption−desorption isotherms and (B) pore size distribution of the ps-PO$_4$Fs.

during phosphate implantation. Therefore, 12 h of implantation time was selected as the optimal time period for the fabrication of ps-PO$_4$Fs, having 11.67% phosphate content. Figure 2A exhibits the XRD patterns of ps-PO$_4$Fs prepared under optimal conditions, in comparison with the vaterite optimal-CaCO$_3$ support. The characteristic peaks of hydroxyapatite (HAp) and the reduced intensities of the vaterite

CaCO$_3$ peaks were observed in the ps-PO$_4$Fs. Figure 2B exhibits FTIR spectra of KH$_2$PO$_4$ powder, optimal-CaCO$_3$, and ps-PO$_4$Fs. Information on the vibrational band position and assignment is summarized in Table S1. For ps-PO$_4$Fs, the main peaks at 1020, 600, and 561 cm^{-1} correspond to PO$_4$ asymmetric stretching and bending, whereas peaks at 874 and
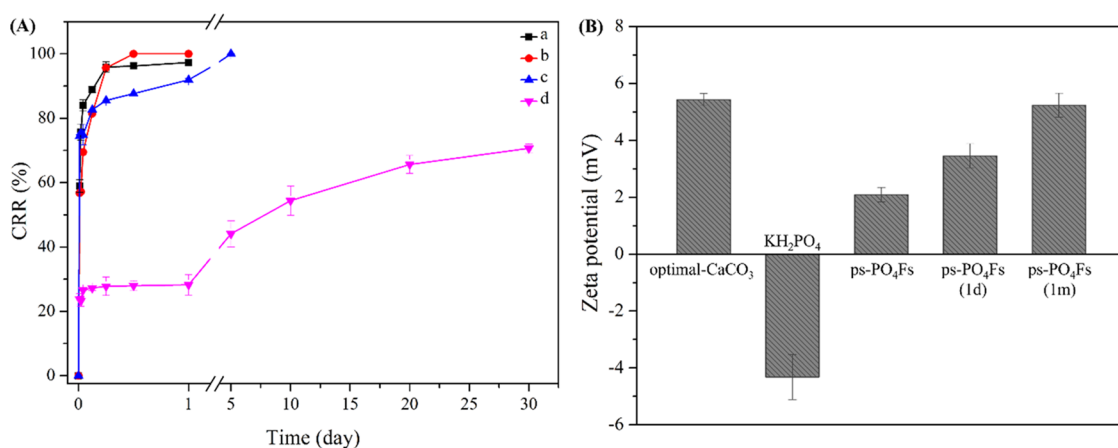
Figure 5. (A) Phosphate release behaviors of (a) KH_2PO_4 powder, (b) DAP, (c) PCFs, and (d) ps-PO_4Fs. (B) Zeta potential of optimal-$CaCO_3$, KH_2PO_4, and ps-PO_4Fs before and after the first-step (ps-PO_4Fs-1d) and second-step release (ps-PO_4Fs-1m).

745 cm^{-1} relate to the CO_3 out-of-plane and in-plane bending, respectively.

The SEM image in Figure 1B shows the surface morphology of the ps-PO_4Fs. Interestingly, the surfaces of the ps-PO_4Fs particles differ significantly from those of the optimal-$CaCO_3$ particles as shown in Figure 1A. Specifically, the prepared ps-PO_4Fs have a porous network structure covering the surface of the optimal-$CaCO_3$ support. The difference in morphologies of these materials could result from the formation of CaP particles deposited on the $CaCO_3$ surface, as confirmed by the FTIR and XRD results. The energy dispersive X-ray (EDX) spectrum in Figure 3A contains a key peak at approximately 2 keV, confirming the presence of phosphorous in the ps-PO_4Fs. The phosphate content in ps-PO_4Fs is equal to 11.51%, consistent with %IC. Moreover, the Ca/P ratio was found to be 3.74. These results demonstrate the successful implantation of phosphate in the form of a porous sponge-like network on the surface of the optimal-$CaCO_3$ particles.

In addition, the presence of phosphate in the ps-PO_4Fs was confirmed by thermogravimetry. As shown in Figure 3B, the TG curve exhibits four stages of weight loss. The initial weight loss from 25 to 200 °C can be ascribed to the dehydration of the ps-PO_4Fs. The second mass loss between 200 and 500 °C could correspond to the decomposition of DCPD and PVA, as well as the formation of pyrophosphate.[32,40,41] The third mass loss from 500 to 700 °C can be attributed to the decomposition of $CaCO_3$. The last weight loss from 700 to 900 °C can be attributed to the decarboxylation of HAp, releasing CO_2.[42,43]

The N_2 adsorption−desorption measurements were carried out to obtain the BET surface areas and pore size distribution of ps-PO_4Fs. Figure 4 presents the isotherms and pore size distribution of the ps-PO_4Fs. It was found that the isotherms of ps-PO_4Fs in Figure 4A are type IV, according to the IUPAC classification, which proves the presence of mesopores in ps-PO_4Fs.[44] Besides, Figure 4B reveals a wide pore size distribution of ps-PO_4Fs. Most pore sizes tend to be found in the diameter range of 10−40 nm, but pores with a 5 nm diameter are also apparent. However, an average pore diameter of ps-PO_4Fs is ~24 nm. The BET results for the ps-PO_4Fs and optimal-$CaCO_3$ are presented in Table S3. As shown, the surface area of ps-PO_4Fs is approximately 22 times greater than that of the optimal-$CaCO_3$ particles, and their pore volume is increased by approximately 14 times. These significant

enhancements in the ps-PO_4Fs result from the porous structure.

3.3. Phosphate Release from ps-PO_4Fs. The phosphate release behavior of ps-PO_4Fs in deionized water was compared with those of KH_2PO_4, DAP, and PCFs, and the %CRR is reported as a function of time over a month. As shown in Figure 5A, the release of phosphate from KH_2PO_4 and DAP was rapid and completed within 6 h. For the PCFs, the phosphate release increased rapidly initially, followed by a slow release for 5 days. Interestingly, we discovered that ps-PO_4Fs exhibited long-term two-step release characteristics. The first release step occurred within a day, having fast release kinetics and reaching a maximum %CRR of approximately 28%. The second continued with a moderate increase up to a month with a maximum %CRR of approximately 70%. These results indicate good slow-controlled release behavior of the ps-PO_4Fs, superior to that of KH_2PO_4 and DAP. In addition, the ps-PO_4Fs exhibited improved slow-release performance compared to PCFs. Crucially, the bimodal release of ps-PO_4Fs is promising for the supply of phosphate to plants at different stages of growth.

Moreover, the zeta potentials of the materials were examined to understand the key interactions between optimal-$CaCO_3$ and KH_2PO_4 as well as the phosphate release process of ps-PO_4Fs in each step. As presented in Figure 5B, the surface charge of the optimal-$CaCO_3$ particles was found to be positive at +5.43 mV, whereas the ps-PO_4Fs particles were found to be positively charged at +2.09 mV. The reduction in the surface charge of ps-PO_4Fs implies the successful implantation of phosphate onto the optimal-$CaCO_3$ support via electrostatic interactions with $H_2PO_4^-/HPO_4^{2-}$ ions in solution and subsequent anion exchange. Additionally, the measurement of the ζ potentials of the ps-PO_4Fs after the release of phosphate in each step revealed the variation in their surface charge. After 1 day (ps-PO_4Fs-1d) and 1 month (ps-PO_4Fs-1m), the surface charges increased to +3.45 and +5.23 mV, respectively. This indicates the continuous release of phosphate from the surfaces of the ps-PO_4Fs. Interestingly, the surface charge of ps-PO_4Fs-1m returned to a slightly lower value than that of the optimal-$CaCO_3$ particles, implying that the majority of the phosphate had been released from the fertilizers.

To understand the mechanism of phosphate release from the ps-PO_4Fs, four kinetic models, first-order, Higuchi, Ritger−

Table 1. Kinetic Fitting Parameters for Each Mathematical Model of Phosphate Release[a]

model parameter	first-order		Higuchi		Ritger–Peppas			parabolic diffusion		
	k	R^2	k	R^2	k	R^2	n	k	R^2	b
KH$_2$PO$_4$ powder	0.0052	0.5724	3.2802	0.7501	84.8895	0.8954	0.0490	102.2897	0.9742	−22.3629
DAP	0.0128	0.5573	7.6710	0.7568	71.6730	0.9036	0.1229	83.0220	0.9845	−16.1392
PCFs	0.0069	0.7285	3.9276	0.8780	75.8349	0.9732	0.0635	91.5073	0.9746	−19.9820
ps-PO$_4$Fs										
1st step	0.0061	0.4266	1.0231	0.8311	25.2711	0.8104	0.0434	**50.3033**	**0.9552**	**−15.9262**
2nd step	0.0012	0.7866	1.9421	0.9755	**11.8672**	**0.9980**	**0.2746**	6.5517	0.9941	−0.1792

[a]Bold values indicate the best fitting model for phosphate release in each step.
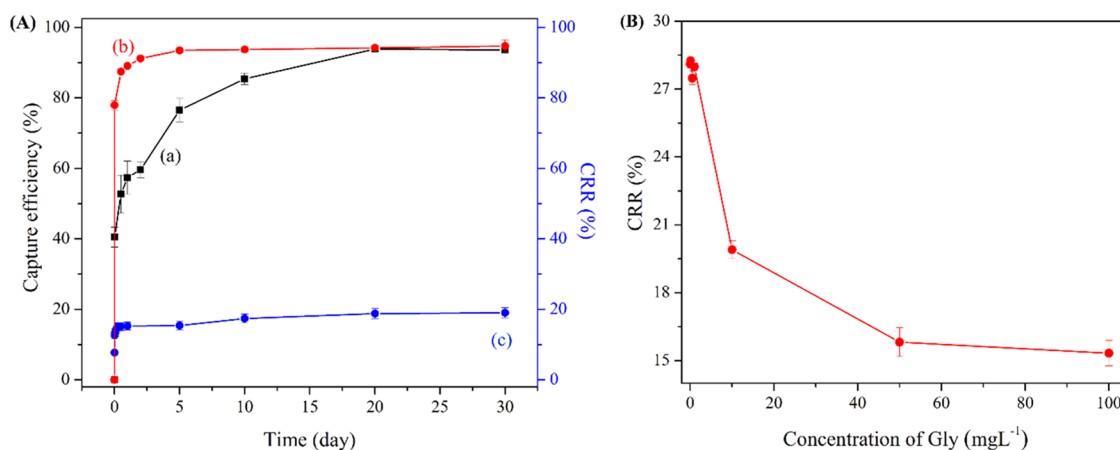

Figure 6. (A) Capture of glyphosate by (a) optimal-CaCO$_3$ and (b) ps-PO$_4$Fs, and (c) phosphate release from ps-PO$_4$Fs in the presence of 100 mg L^{-1} glyphosate. (B) Effect of glyphosate concentration on the release of phosphate from ps-PO$_4$Fs.

Peppas, and parabolic diffusion, were used to fit the data. The plots for these kinetic models are provided in Figure S12 for KH$_2$PO$_4$, DAP, PCFs, and ps-PO$_4$Fs (first release step), and Figure S13 for ps-PO$_4$Fs (second release step). The corresponding parameters for each model are listed in Table 1. The results indicate that the release of phosphate from KH$_2$PO$_4$, DAP, and PCFs follows a parabolic diffusion model with kinetic constants (k) of 102.29, 83.02, and 91.51, respectively. These results confirm a fast release of phosphate from these fertilizers into the solution, as seen in Figure 5A. For ps-PO$_4$Fs, a two-step release was observed. As for the other fertilizers, the first stage of release of phosphate from ps-PO$_4$Fs corresponds to the parabolic diffusion model with a k value of 50.30, which is lower than those of the other fertilizers. Thus, the first stage of phosphate release from ps-PO$_4$Fs could be controlled by an external surface/edge diffusion process.[45] This implies the diffusion of phosphate from the surfaces of the ps-PO$_4$Fs particles into solution and the release rate could be dependent on their dissolution. For the second stage of phosphate release, the data correspond well to the Ritger–Peppas model, having a k value of 12.33 and n of 0.2746. A slow phosphate release in this stage was associated with the diffusion of phosphate adsorbed at pore sites of ps-PO$_4$Fs, according to Fickian diffusion ($n < 0.43$).[45,46] These results demonstrate that a bimodal controlled release of composite fertilizer with different kinetics, a first fast-release step in the first 24 h and a second slow-release step over the course of a month, can be achieved by the proposed fabrication method.

Next, XRD and FTIR measurements were performed to determine the structural changes in ps-PO$_4$Fs after phosphate release. As shown in Figure S14, the XRD patterns of ps-PO$_4$Fs after the first release step (ps-PO$_4$Fs-1d) and second step (ps-

PO$_4$Fs-1m) remained the same. This implies that the diffusion of phosphate from the surfaces of the ps-PO$_4$Fs particles did not affect the crystal phase. As expected, a reduced intensity of characteristic peaks of phosphate, at $2\theta = 45.26$ and $57.78°$, in both ps-PO$_4$Fs-1d and ps-PO$_4$Fs-1m was observed as a result of phosphate release. However, the peak intensities in the pattern of the ps-PO$_4$Fs-1m were higher than those in the pattern of the ps-PO$_4$Fs-1d. This was probably due to more phosphate release from ps-PO$_4$Fs through a dissolution over 1 month, which could result in the change of their elemental composition. In addition, the characteristic peaks of PO$_4$ and CaCO$_3$ were observed in the FTIR spectra of ps-PO$_4$Fs before and after phosphate release, as displayed in Figure S15 with vibrational band position and assignment in Table S4. The result specifies an incomplete release of phosphate over the studied period of 1 month, as shown in Figure 5A. This also implies that the fabricated ps-PO$_4$Fs do not affect the water hardness during phosphate release, showing their advantage for practical use.

3.4. Double Functionality of ps-PO$_4$Fs. Because of their porous structure, the feasibility of using the ps-PO$_4$Fs for capturing compounds was investigated. In this study, glyphosate was selected as a representative herbicide that is widely used in agriculture. The chemical structure of glyphosate is given in Figure S16. The ability of the ps-PO$_4$Fs particles to capture glyphosate in comparison with the optimal-CaCO$_3$ particles was first examined at a glyphosate concentration of 100 mg L^{-1}. As shown in Figure 6A, the rate of adsorption of glyphosate of ps-PO$_4$Fs was significantly greater than that of optimal-CaCO$_3$. Further, the ps-PO$_4$Fs reached a capture efficiency of approximately 94% after 5 days, whereas optimal-CaCO$_3$ took 20 days to reach the same level.
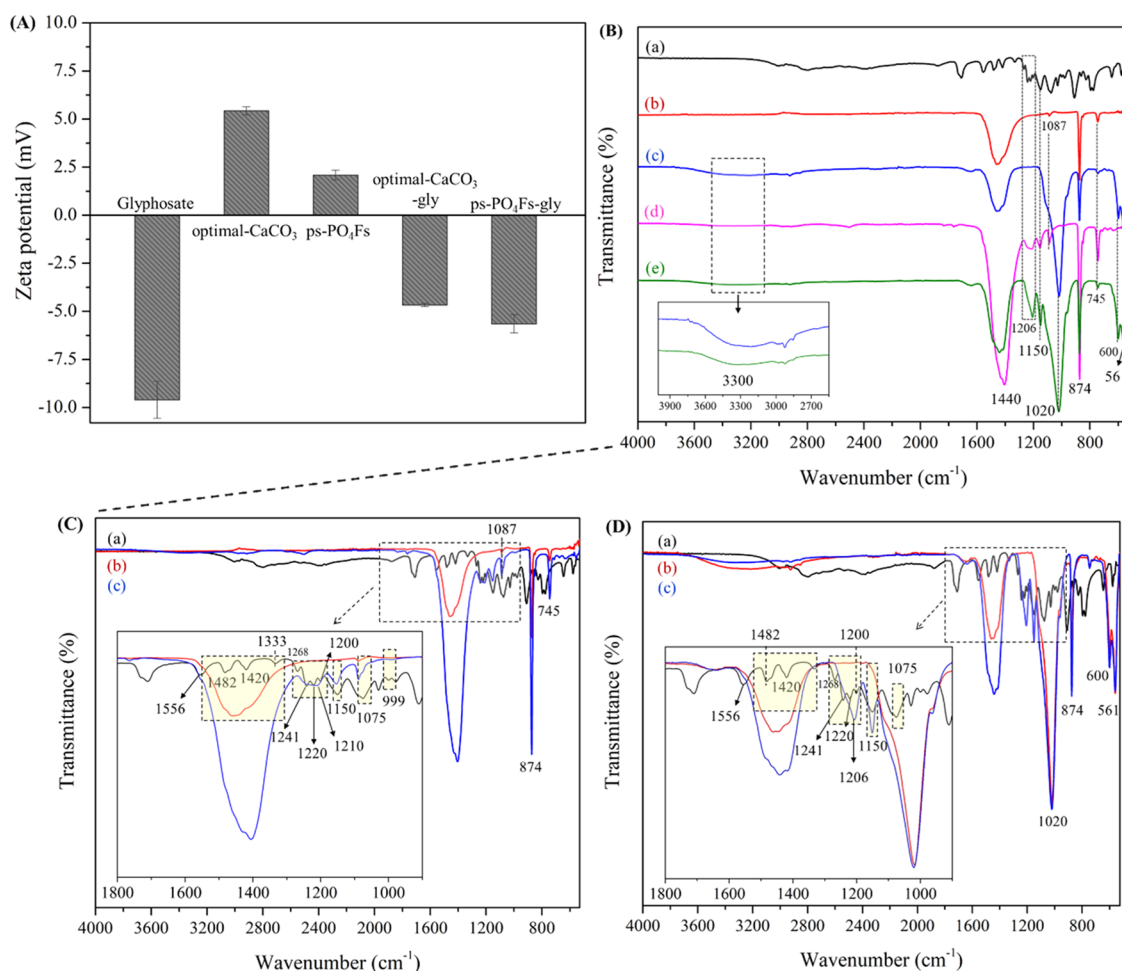
Figure 7. (A) ζ Potential of samples and (B) FTIR spectra of (a) glyphosate, (b) optimal-CaCO$_3$, (c) ps-PO$_4$Fs, (d) optimal-CaCO$_3$-gly, and (e) ps-PO$_4$Fs-gly. Plots for comparison of (C) FTIR spectra of (a) glyphosate, (b) optimal-CaCO$_3$, and (c) optimal-CaCO$_3$-gly, and (D) FTIR spectra of (a) glyphosate, (b) ps-PO$_4$Fs, and (c) ps-PO$_4$Fs-gly.

This finding can be explained by the larger surface area of the ps-PO$_4$Fs compared to that of optimal-CaCO$_3$, as shown by the data in Table S3. In addition, we found that the adsorption of glyphosate on the ps-PO$_4$Fs surface inhibited phosphate release. Specifically, phosphate release was only approximately 15% when the adsorption of glyphosate was over 80% (about 28% in the absence of glyphosate, as shown in Figure 5A). Thus, glyphosate adsorption significantly affects the phosphate release characteristics of ps-PO$_4$Fs.

To understand the effects of glyphosate concentration on phosphate release further, different glyphosate concentrations were used, and the phosphate release was monitored over a 24 h period (Figure 6B). A slight decrease in phosphate release from the ps-PO$_4$Fs was observed at low glyphosate concentrations. However, a noteworthy decrease in phosphate release (approximately 20%) was observed when the concentration of glyphosate increased to 10 mg L^{-1}, possibly because of the high coverage of glyphosate on the surfaces of the pores in the ps-PO$_4$Fs at this concentration. Thus, at high concentrations, the diffusion of phosphate from the ps-PO$_4$Fs was hindered, and, at the highest glyphosate concentration (100 mg L^{-1}), almost 50% reduction in the phosphate release efficiency was observed. In summary, the functional ps-PO$_4$Fs having fast and slow phosphate release modes are advantageous for the growth of plants over long periods, and their

excellent adsorption ability for compounds such as glyphosate could enable their use for environmental remediation.

Next, the zeta potential was measured and FTIR measurements were used to confirm the interaction between the prepared samples and glyphosate. As shown in Figure 7A, the surfaces of the ps-PO$_4$Fs particles are less positively charged than those of the optimal-CaCO$_3$ particles, whereas glyphosate molecules are negatively charged in solution. Therefore, glyphosate can be adsorbed on the surface of both materials via electrostatic interactions. However, a stronger interaction with glyphosate is expected for the ps-PO$_4$Fs particles because of their nanoscale pores and large specific surface area. Moreover, a chelation of glyphosate with Ca^{2+} of ps-PO$_4$Fs could occur and accelerate the adsorption process. Consequently, the surface charge of ps-PO$_4$Fs-gly is more negative than that of optimal-CaCO$_3$-gly. This implies a greater adsorption capacity of ps-PO$_4$Fs toward glyphosate. Figure 7B shows the FTIR spectra of all samples. The bands of glyphosate were found at 999, 1075, 1150, 1220, and 1268 cm^{-1}; 1200, 1420, and 1710 cm^{-1}; 1482 and 1556 cm^{-1}; and 979, 1241, and 1333 cm^{-1}, which are attributed to the glyphosate phosphate group, carboxylic group, amine group, and CH$_2$ group, respectively.[47,48] Figure 7C,D presents the plots of the FTIR spectra for comparison to evaluate the interaction between samples and glyphosate. For the optimal-
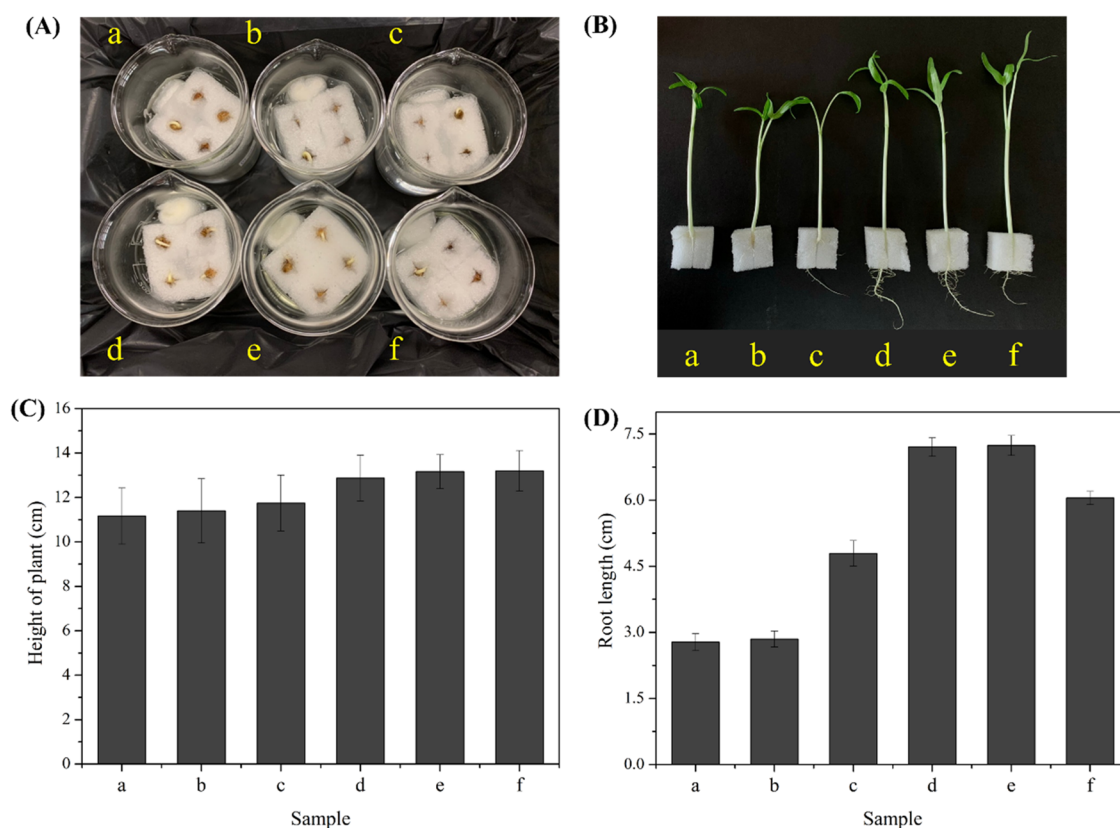
Figure 8. (A) Setup and seed germination after a day, (B) a digital photograph of *I. aquatica* after a week, and (C) plant height and (D) length of root after growth in (a) deionized water and water supplemented with (b) optimal-CaCO$_3$, (c) PCFs, (d) KH$_2$PO$_4$, (e) DAP, and (f) ps-PO$_4$Fs. Photos were taken by Pratchayaporn Yukhajon.

CaCO$_3$, characteristic peaks at 1087, 874, and 745 cm^{-1} can be seen in Figure 7C, and these are related to the symmetric stretching and out-of-plane and in-plane bending vibrations of carbonate, respectively.[49] After adsorption of 100 mg L^{-1} glyphosate (samples are denoted with an appended "-gly"), characteristic peaks in the spectrum of optimal-CaCO$_3$-gly appeared at 1075 and 1150 cm^{-1}, and this can be attributed to the phosphonate group of glyphosate. The broad peak at 1241 cm^{-1} (overlap) corresponds to the −CH$_2$ group of glyphosate. Notably, the peaks at 1268 and 1220 cm^{-1}, which corresponds to the phosphonate group of glyphosate shifted to 1210 cm^{-1}, probably because of hydrogen bonding interactions between the −OH group of optimal-CaCO$_3$ and P=O and P−O$^-$ (PO$_3^{2-}$ group) of glyphosate, respectively.[48,50] However, the characteristics peaks of glyphosate at 1482 and 1420 cm^{-1}, attributed to the vibration of the amine group and C−OH (carboxylic group), respectively, were unable to be identified due to the overlapping with carbonate bands. In other words, the C−O$^-$ (carboxylate group) of glyphosate can form a complex with Ca^{2+} of optimal-CaCO$_3$, which can lead to the peak shifting to around 1400 cm^{-1} (overlapping peak) in the optimal-CaCO$_3$-gly.[51] For ps-PO$_4$Fs, characteristic peaks at 1020, 600, and 561 cm^{-1} were observed in Figure 7D. These peaks were assigned to the phosphate groups, and additional peaks at 874 and 745 cm^{-1} related to the out-of-plane and in-plane bending, respectively. Vibrations of carbonate groups were also observed. After the adsorption of glyphosate, the FTIR pattern of ps-PO$_4$Fs-gly showed characteristic peaks at 1150 and 1075 (overlap), and 999 cm^{-1} (overlap), corresponding to the phosphonate group of glyphosate.[48,50]

The peak at 1241 cm^{-1} (shoulder) corresponding to the −CH$_2$ group of glyphosate was also found. Remarkably, the peaks at 1268 and 1220 cm^{-1}, which are related to the phosphonate group, shifted to 1206 cm^{-1}.[48,50] Also, the relative intensity of the peak at 3300 cm^{-1} corresponding to the vibrations of −OH groups in ps-PO$_4$Fs-gly decreased, compared to that in the spectrum of the ps-PO$_4$Fs. These observations in ps-PO$_4$Fs-gly can be explained as resulting from the formation of hydrogen bonds between P=O and P−O$^-$ of glyphosate and −OH group of ps-PO$_4$Fs. Similar to optimal-CaCO$_3$-gly, the characteristic peaks of glyphosate were unidentifiable in ps-PO$_4$Fs-gly due to the peak overlapping. These results reconfirm the interaction between ps-PO$_4$Fs and glyphosate, which could affect dose-dependent phosphate release kinetics of ps-PO$_4$Fs.

3.5. Use of ps-PO$_4$Fs for Plant Growth. The applications of ps-PO$_4$Fs were tested using *I. aquatica*, a plant that grows in water or moist soil. All experiments were conducted in the laboratory. Figure 8A shows the experimental setup, in which seeds of *I. aquatica* were placed inside a sponge floating above the fertilizer suspension. Seed germination occurred after 1 day, and was carried out under identical conditions with deionized water, optimal-CaCO$_3$, PCFs, KH$_2$PO$_4$, DAP, and ps-PO$_4$Fs. Figure 8B shows a photograph of the plant growth after a week. The efficiency of each fertilizer is reported in terms of plant height and root length after a week. As shown in Figure 8C, comparable plant heights were achieved for plants supplemented with KH$_2$PO$_4$, DAP, and ps-PO$_4$Fs. Concerning the length of plant roots (Figure 8D), the experiments carried out with rapidly dissolved KH$_2$PO$_4$ and DAP yielded longer

and hairier roots compared to the use of the other fertilizers. In contrast, root growth was inhibited in the phosphate-deficient system. When using the ps-PO$_4$Fs, good plant and root growth was observed, and the sustained release of phosphate from ps-PO$_4$Fs could potentially satisfy the fertilizer needs of plants for longer periods than those tested. These results demonstrate that ps-PO$_4$Fs have promise for use as efficient fertilizers and have an almost equivalent effect to commercial fertilizers. However, further studies of the ps-PO$_4$Fs in complex soil environment using other plant species as well as the effect of pH and some interfering agents such as common salts and minerals or typical organic components are also required.

4. CONCLUSIONS

This work presents a simple strategy for the fabrication of functional phosphate/carbonate composites for use as fertilizers with improved controlled-release and adsorption ability toward glyphosate. The preparation of the composites involved the implantation of phosphate onto the surface of vaterite-phase CaCO$_3$ supports through an anion exchange process. The obtained composite fertilizers have a nanoporous network structure with a large specific surface area. A study of the phosphate release of the fertilizers revealed that they have two distinct modes of release and that phosphate release does not alter the crystal phase of CaCO$_3$. The two release steps showed different release kinetic characteristics: the first step was fast and occurred over 24 h, whereas the latter was much slower over a month. In addition, these fertilizers had good adsorption toward glyphosate because of their porous structure. Further, only high concentrations of glyphosate resulted in its rapid and dominant adsorption in the pores of the particles and, thus, the reduced diffusion of phosphate. Moreover, the practical use of fertilizers was found to be efficient for plant growth. Thus, these smart, eco-friendly, and multifunctional fertilizers have great potential for agricultural use. They are promising not only for use as plant-growth supplements but also for environmental remediation. In particular, the two-step phosphate release over a long-term period is useful because it avoids the initial rapid release of phosphate at levels that cannot be absorbed by plants, suggesting that these fertilizers could increase the sustainability and environmental friendliness of current agricultural practices. Still, further studies and development of the fertilizers for efficient use in soil environment with other plants are necessary.

ASSOCIATED CONTENT

Supporting Information

The Supporting Information is available free of charge at https://pubs.acs.org/doi/10.1021/acsomega.2c00425.

> SEM images, XRD patterns, FTIR spectra, TGA/DTG curves of samples, plots of %IC for fabrication of composites, plots for kinetic models for phosphate release of materials, and FTIR peak assignment of materials (PDF)

AUTHOR INFORMATION

Corresponding Author

Sira Sansuk − Materials Chemistry Research Center, Department of Chemistry and Center of Excellence for Innovation in Chemistry, Faculty of Science, Khon Kaen University, Khon Kaen 40002, Thailand; orcid.org/0000-0001-5691-8775; Email: sirisan@kku.ac.th

Authors

Pratchayaporn Yukhajon − Materials Chemistry Research Center, Department of Chemistry and Center of Excellence for Innovation in Chemistry, Faculty of Science, Khon Kaen University, Khon Kaen 40002, Thailand

Titikan Somboon − Department of Chemistry, Faculty of Engineering, Rajamangala University of Technology Isan, Khon Kaen 40000, Thailand

Complete contact information is available at:
https://pubs.acs.org/10.1021/acsomega.2c00425

Author Contributions

All authors contributed to and approved the manuscript.

Notes

The authors declare no competing financial interest.

■ REFERENCES

(1) Everaert, M.; Warrinnier, R.; Baken, S.; Gustafsson, J.-P.; De Vos, D.; Smolders, E. Phosphate-Exchanged Mg−Al Layered Double Hydroxides: A New Slow Release Phosphate Fertilizer. ACS Sustainable Chem. Eng. 2016, 4, 4280−4287.

(2) Weiner, E. R. Applications of Environmental Aquatic Chemistry: A Practical Guide, 3rd ed.; CRC Press, 2012; p 456.

(3) Barker, A. V.; Pilbeam, D. J. Handbook of Plant Nutrition; CRC Press, 2016; p 632.

(4) Yi, Y.; Xu, S.; Sun, H.; Chang, D.; Yin, Y.; Zheng, H.; Xu, H.; Lou, Y. Gelation of Photocrosslinkable Carboxymethyl Chitosan and Its Application in Controlled Release of Pesticide. Carbohydr. Polym. 2011, 86, 1007−1013.

(5) Cao, L.; Zhang, H.; Cao, C.; Zhang, J.; Li, F.; Huang, Q. Quaternized Chitosan-Capped Mesoporous Silica Nanoparticles as Nanocarriers for Controlled Pesticide Release. Nanomaterials 2016, 6, No. 126.

(6) Hart, M. R.; Quin, B. F.; Nguyen, M. L. Phosphorus Runoff from Agricultural Land and Direct Fertilizer Effects: A Review. J. Environ. Qual. 2004, 33, 1954−1972.

(7) Vejan, P.; Khadiran, T.; Abdullah, R.; Ahmad, N. Controlled release fertilizer: A Review on Developments, Applications and Potential in Agriculture. J. Control Release 2021, 339, 321−334.

(8) Duke, S. O.; Reddy, K. N.; Bu, K.; Cizdziel, J. V. Effects of Glyphosate on the Mineral Content of Glyphosate-Resistant Soybeans (Glycine max). J. Agric. Food Chem. 2012, 60, 6764−6771.

(9) Smedbol, E.; Lucotte, M.; Maccario, S.; Gomes, M. P.; Paquet, S.; Moingt, M.; Mercier, L. L. C.; Sobarzo, M. R. P.; Blouin, M.-A. Glyphosate and Aminomethylphosphonic Acid Content in Glyphosate-Resistant Soybean Leaves, Stems, and Roots and Associated Phytotoxicity Following a Single Glyphosate-Based Herbicide Application. J. Agric. Food Chem. 2019, 67, 6133−6142.

(10) Li, Z.-Z.; Xu, S.-A.; Wen, L.-X.; Liu, F.; Liu, A.-Q.; Wang, Q.; Sun, H.-Y.; Yu, W.; Chen, J.-F. Controlled Release of Avermectin from Porous Hollow Silica Nanoparticles: Influence of Shell Thickness on Loading Efficiency, UV-Shielding Property and Release. J. Control Release 2006, 111, 81−88.

(11) Qu, R.; Zhang, W.; Liu, N.; Zhang, Q.; Liu, Y.; Li, X.; Wei, Y.; Feng, L. Antioil Ag$_3$PO$_4$ Nanoparticle/Polydopamine/Al$_2$O$_3$ Sandwich Structure for Complex Wastewater Treatment: Dynamic Catalysis under Natural Light. ACS Sustainable Chem. Eng. 2018, 6, 8019−8028.

(12) Chi, Y.; Zhang, G.; Xiang, Y.; Cai, D.; Wu, Z. Fabrication of a Temperature-Controlled-Release Herbicide Using a Nanocomposite. *ACS Sustainable Chem. Eng.* **2017**, *5*, 4969−4975.

(13) Meftaul, I. M.; Venkateswarlu, K.; Dharmarajan, R.; Annamalai, P.; Asaduzzaman, M.; Parven, A.; Megharaj, M. Controversies over Human Health and Ecological Impacts of Glyphosate: Is It to be Banned in Modern Agriculture? *Environ. Pollut.* **2020**, *263*, No. 114372.

(14) Jarosiewicz, A.; Tomaszewska, M. Controlled-Release NPK Fertilizer Encapsulated by Polymeric Membranes. *J. Agric. Food Chem.* **2003**, *51*, 413−417.

(15) Ni, B.; Liu, M.; Lü, S. Multifunctional Slow-Release Urea Fertilizer from Ethylcellulose and Superabsorbent Coated Formulations. *Chem. Eng. J.* **2009**, *155*, 892−898.

(16) Karunarathna, M. H. J. S.; Hatten, Z. R.; Bailey, K. M.; Lewis, E. T.; Morris, A. L.; Kolk, A. R.; Laib, J. C.; Tembo, N.; Williams, R. A.; Phillips, B. T.; Ash, B. L.; Midden, W. R.; Ostrowski, A. D. Reclaiming Phosphate from Waste Solutions with Fe(III)−Poly-saccharide Hydrogel Beads for Photo-Controlled-Release Fertilizer. *J. Agric. Food Chem.* **2019**, *67*, 12155−12163.

(17) da Cruz, D. F.; Bortoletto-Santos, R.; Guimarães, G. G. F.; Polito, W. L.; Ribeiro, C. Role of Polymeric Coating on the Phosphate Availability as a Fertilizer: Insight from Phosphate Release by Castor Polyurethane Coatings. *J. Agric. Food Chem.* **2017**, *65*, 5890−5895.

(18) Qi, T.; Lü, S.; Zhang, S.-F.; Bai, X.; Chen, J.; Huang, M.; Liu, M. Zein Coated Porous Carboxymethyl Starch Fertilizer for Iron Promoting and Phosphate Sustainable Release. *J. Cleaner Prod.* **2020**, *258*, No. 120778.

(19) Wang, Z.; Lu, J.; Wu, C. Preparation of Fe-filled MOF-Al-based Hydrogel for Efficient Reclaim of Phosphate From Wastewater and Reusing as a Slow-release Fertilizer. *Environ. Technol.* **2021**, 1−12.

(20) Bernardo, M. P.; Guimarães, G. G. F.; Majaron, V. F.; Ribeiro, C. Controlled Release of Phosphate from Layered Double Hydroxide Structures: Dynamics in Soil and Application as Smart Fertilizer. *ACS Sustainable Chem. Eng.* **2018**, *6*, 5152−5161.

(21) Li, J.; Jiang, H.; Ouyang, X.; Han, S.; Wang, J.; Xie, R.; Zhu, W.; Ma, N.; Wei, H.; Jiang, Z. CaCO₃/Tetraethylenepentamine−Graphene Hollow Microspheres as Biocompatible Bone Drug Carriers for Controlled Release. *ACS Appl. Mater. Interfaces* **2016**, *8*, 30027−30036.

(22) Ferreira, A. M.; Vikulina, A. S.; Volodkin, D. CaCO₃ Crystals as Versatile Carriers for Controlled Delivery of Antimicrobials. *J. Control Release* **2020**, *328*, 470−489.

(23) Zhang, J.; Li, Y.; Xie, H.; Su, B.-L.; Yao, B.; Yin, Y.; Li, S.; Chen, F.; Fu, Z. Calcium Carbonate Nanoplate Assemblies with Directed High-Energy Facets: Additive-Free Synthesis, High Drug Loading, and Sustainable Releasing. *ACS Appl. Mater. Interfaces* **2015**, *7*, 15686−15691.

(24) Xiang, Y.; Han, J.; Zhang, G.; Zhan, F.; Cai, D.; Wu, Z. Efficient Synthesis of Starch-Regulated Porous Calcium Carbonate Micro-spheres as a Carrier for Slow-Release Herbicide. *ACS Sustainable Chem. Eng.* **2018**, *6*, 3649−3658.

(25) Gissawong, N.; Sansuk, S.; Srijaranai, S. The Alternative Use of Layered Double Hydroxides as Extraction Medium Coupled with Microcomplexation for Determination of Phosphate in Water samples. *Spectrochim. Acta, Part A* **2017**, *173*, 994−1000.

(26) Won, Y.-H.; Jang, H. S.; Chung, D.-W.; Stanciu, L. A. Multifunctional Calcium Carbonate Microparticles: Synthesis and Biological Applications. *J. Mater. Chem.* **2010**, *20*, 7728−7733.

(27) Mansur, H. S.; Sadahira, C. M.; Souza, A. N.; Mansur, A. A. P. FTIR Spectroscopy Characterization of Poly(vinyl alcohol) Hydrogel with Different Hydrolysis Degree and Chemically Crosslinked with Glutaraldehyde. *Mater. Sci. Eng., C* **2008**, *28*, 539−548.

(28) Soni, S. R.; Bhunia, B. K.; Kumari, N.; Dan, S.; Mukherjee, S.; Mandal, B. B.; Ghosh, A. Therapeutically Effective Controlled Release Formulation of Pirfenidone from Nontoxic Biocompatible Carbox-ymethyl Pullulan-Poly(vinyl alcohol) Interpenetrating Polymer Networks. *ACS Omega* **2018**, *3*, 11993−12009.

(29) Guo, B.; Zhao, T.; Sha, F.; Zhang, F.; Li, Q.; Zhang, J. Control over Crystallization of CaCO₃ Micro-particles by a Novel CO₂SM. *CrystEngComm* **2015**, *17*, 7896−7904.

(30) Hossain, U. H.; Seidl, T.; Ensinger, W. Combined In situ Infrared and Mass Spectrometric Analysis of High-energy Heavy Ion Induced Degradation of Polyvinyl Polymers. *Polym. Chem.* **2014**, *5*, 1001−1012.

(31) Safaee-Ardakani, M. R.; Hatamian-Zarmi, A.; Sadat, S. M.; Mokhtari-Hosseini, Z. B.; Ebrahimi-Hosseinzadeh, B.; Rashidiani, J.; Kooshki, H. Electrospun Schizophyllan/Polyvinyl Alcohol Blend Nanofibrous Scaffold as Potential Wound Healing. *Int. J. Biol. Macromol.* **2019**, *127*, 27−38.

(32) Awada, H.; Daneault, C. Chemical Modification of Poly(Vinyl Alcohol) in Water. *Appl. Sci.* **2015**, *5*, 840−850.

(33) Gheisari, H.; Karamian, E.; Abdellahi, M. A novel hydroxyapatite −Hardystonite Nanocomposite Ceramic. *Ceram. Int.* **2015**, *41*, 5967−5975.

(34) Xia, X.; Chen, J.; Shen, J.; Huang, D.; Duan, P.; Zou, G. Synthesis of Hollow Structural Hydroxyapatite with Different Morphologies Using Calcium Carbonate as Hard Template. *Adv. Powder Technol.* **2018**, *29*, 1562−1570.

(35) Pham Minh, D.; Lyczko, N.; Sebei, H.; Nzihou, A.; Sharrock, P. Synthesis of Calcium Hydroxyapatite from Calcium Carbonate and Different Orthophosphate Sources: A Comparative Study. *Mater. Sci. Eng., B* **2012**, *177*, 1080−1089.

(36) Rey, C.; Combes, C. 3-Physical Chemistry of Biological Apatites. *Biominer. Biomater.* **2016**, 95−127.

(37) Pham Minh, D.; Tran, N. D.; Nzihou, A.; Sharrock, P. One-Step Synthesis of Calcium Hydroxyapatite from Calcium Carbonate and Orthophosphoric Acid under Moderate Conditions. *Ind. Eng. Chem. Res.* **2013**, *52*, 1439−1447.

(38) Guo, Y.-P.; Yao, Y.-b.; Ning, C.-Q.; Guo, Y.-J.; Chu, L.-F. Fabrication of Mesoporous Carbonated Hydroxyapatite Microspheres by Hydrothermal Method. *Mater. Lett.* **2011**, *65*, 2205−2208.

(39) Guo, Y.-P.; Guo, L.-H.; Yao, Y.-b.; Ning, C.-Q.; Guo, Y.-J. Magnetic Mesoporous Carbonated Hydroxyapatite Microspheres with Hierarchical Nanostructure for Drug Delivery Systems. *Chem. Commun.* **2011**, *47*, 12215−12217.

(40) Wikholm, N. W.; Beebe, R. A.; Kittelberger, J. S. Kinetics of The Conversion of Monetite to Calcium Pyrophosphate. *J. Phys. Chem. A* **1975**, *79*, 853−856.

(41) Pham Minh, D.; Martinez, M. G.; Nzihou, A.; Sharrock, P. Thermal Behavior of Apatitic Calcium Phosphates Synthesized from Calcium Carbonate and Orthophosphoric Acid or Potassium Dihydrogen Orthophosphate. *J. Therm. Anal. Calorim.* **2013**, *112*, 1145−1155.

(42) Meejoo, S.; Maneeprakorn, W.; Winotai, P. Phase and Thermal Stability of Nanocrystalline Hydroxyapatite Prepared via Microwave Heating. *Thermochim. Acta* **2006**, *447*, 115−120.

(43) Yasukawa, A.; Kandori, K.; Ishikawa, T. TPD-TG-MS Study of Carbonate Calcium Hydroxyapatite Particles. *Calcif. Tissue Int.* **2003**, *72*, 243−250.

(44) Alothman, Z. A. A Review: Fundamental Aspects of Silicate Mesoporous Materials. *Materials* **2012**, *5*, 2874−2902.

(45) Dai, C.-F.; Tian, D.-Y.; Li, S.-P.; Li, X.-D. Methotrexate Intercalated Layered Double Hydroxides with The Mediation of Surfactants: Mechanism Exploration and Bioassay Study. *Mater. Sci. Eng., C* **2015**, *57*, 272−278.

(46) Ritger, P. L.; Peppas, N. A. A Simple Equation for Description of Solute Release I. Fickian and Non-Fickian Release from Non-Swellable Devices in The Form of Slabs, Spheres, Cylinders or Discs. *J. Control Release* **1987**, *5*, 23−36.

(47) Miano, T. M.; Piccolo, A.; Celano, G.; Senesi, N. Infrared and Fluorescence Spectroscopy of Glyphosate-Humic Acid Complexes. *Sci. Total Environ.* **1992**, *123−124*, 83−92.

(48) de Santana, H.; Toni, L. R. M.; Benetoli, L. O. dB.; Zaia, C. T. B. V.; Rosa, M.; Zaia, D. A. M. Effect in Glyphosate Adsorption on Clays and Soils Heated and Characterization by FT−IR Spectroscopy. *Geoderma* **2006**, *136*, 738−750.

(49) Chakrabarty, D.; Mahapatra, S. Aragonite Crystals with Unconventional Morphologies. *J. Mater. Chem.* **1999**, *9*, 2953−2957.

(50) Herath, I.; Kumarathilaka, P.; Al-Wabel, M. I.; Abduljabbar, A.; Ahmad, M.; Usman, A. R. A.; Vithanage, M. Mechanistic Modeling of Glyphosate Interaction with Rice Husk Derived Engineered Biochar. *Microporous Mesoporous Mater.* **2016**, *225*, 280−288.

(51) Braschi, I.; Blasioli, S.; Lavrnić, S.; Buscaroli, E.; Di Prodi, K.; Solimando, D.; Toscano, A. Removal and Fate of Pesticides in A Farm Constructed Wetland for Agricultural Drainage Water Treatment Under Mediterranean Conditions (Italy). *Environ. Sci. Pollut. Res.* **2022**, *29*, 7283−7299.